CHEMISTRY OF MATERIALS
Article

Chem. Mater. **2010,** *22,* 3033–3042 3033
DOI:10.1021/cm100181c

Ordered Arrays of Bead-Chain-like In_2O_3 Nanorods and Their Enhanced Sensing Performance for Formaldehyde

Xiaoyong Lai,[†] Dan Wang,*[,†] Ning Han,[†] Jiang Du,[†] Jun Li,[†] Chaojian Xing,[†] Yunfa Chen,[†] and Xiaotian Li[‡]

[†]*State Key Laboratory of Multi-phase Complex Systems, Institute of Process Engineering, Chinese Academy of Sciences, Beijing 100190, P. R. China., and* [‡]*College of Materials Science and Engineering, Jilin University, Changchun 130012, P. R. China*

Received June 27, 2009. Revised Manuscript Received April 16, 2010

Here we present a class of formaldehyde (HCHO) gas sensors with strong responses based on ordered mesostructured In_2O_3 nanorod arrays, which are synthesized via the nanocasting route by directly using the solvent-extracted mesoporous silica as a hard template. By choosing mesoporous silica with different pore sizes and interconnectivity as templates and varying the loading of indium resource on the silica template, we have obtained a series of mesostructured In_2O_3 nanorod arrays with different textural parameters such as specific surface area, pore size, nanorod diameter, etc. The gas sensing properties for formaldehyde (HCHO) of the In_2O_3 specimens were examined. The results reveal those mesostructured In_2O_3 nanorod arrays possess much stronger responses to HCHO even at low concentrations than the bulk In_2O_3, and larger specific surface areas and pore sizes as well as smaller nanorod diameters would be beneficial for enhancing the sensing properties of In_2O_3.

Introduction

The growing concern about the consequences of air pollution with respect to public health has enhanced the demand for gas sensors for monitoring air quality and stimulated much interest in related research.[1,2] Semiconductor-based gas sensors offer good advantages with respect to others because of their simple implementation, low cost, short response time, and good suitability for the design of portable instruments.[3−5] The fundamental mechanism of semiconductor gas sensors is based on the change in electrical conductivity due to the surface−chemical interaction between the crystalline sensor material and gas molecules absorbed on the surface, whose sensing performances strongly depend on their surface-to-volume ratio. Over the past few decades, much effort has been devoted to the investigation of nanocrystalline sensors with reduced grain size, and their large surface-to-volume ratio is expected to allow for high-performance sensing.[6,7] However, some inherent restrictions such as gas diffusion inside the sensors, grain agglomeration, and loss of specific surface area resulting from sintering in the process and operation must be resolved. Individual nanowire sensors offer an attractive alternative to avoid these restrictions.[8,9] Furthermore, the direct influence of the nanowire transverse diameter on the sensor response has also been reported.[10] According to these results, the response toward gases sharply increases with a decreasing transverse diameter below 15 nm. In this case, the conduction channel along the nanowire is close to complete depletion, and small variations in the charge trapped at the surface by gaseous molecules lead to huge effects on their electrical responses. Typical sizes for depleted regions in metal oxides are close to 3−5 nm.[11] Therefore, ultrathin nanowires less than 10 nm in diameter are considered excellent candidates for studying deep depletion effects, understanding the complete shrinkage of the conductive channel, and fabricating a high-performance gas sensor. Unfortunately, further development is still hindered by the difficulty in synthesizing ultrathin nanowires and technical drawbacks with respect to manipulating and electrically contacting individual ultrathin nanowires.

Recently, significant progress has been achieved in the preparation of mesoporous metal oxides with crystalline

*To whom correspondence should be addressed. Fax: +86 10 62631141. Telephone: +86 10 62533616. E-mail: danwang@home.ipe.ac.cn.

(1) Baraton, M.; Merhari, L. *Rev. Adv. Mater. Sci.* **2003**, *4*, 15–24.
(2) Yamazoe, N.; Shimanoe, K. *Sens. Actuators, B* **2009**, *138*, 100–107.
(3) Persaud, K.; Dodd, G. *Nature* **1982**, *299*, 352–355.
(4) Li, Z. M.; Lai, X. Y.; Wang, H.; Mao, D.; Xing, C. J.; Wang, D. *J. Phys. Chem. C* **2009**, *113*, 2792–2797.
(5) Li, X. L.; Lou, T. J.; Sun, X. M.; Li, Y. D. *Inorg. Chem.* **2004**, *43*, 5442–5449.
(6) Cao, M.; Wang, Y.; Chen, T.; Antonietti, M.; Niederberger, M. *Chem. Mater.* **2008**, *20*, 5781–5786.
(7) McCue, J. T.; Ying, J. Y. *Chem. Mater.* **2007**, *19*, 1009–1015.
(8) Kolmakov, A.; Klenov, D.; Lilach, Y.; Stemmer, S.; Moskovits, M. *Nano Lett.* **2005**, *5*, 667–673.
(9) Hernandez-Ramirez, F.; Tarancon, A.; Casals, O.; Pellicer, E.; Rodriguez, J.; Romano-Rodriguez, A.; Morante, J.; Barth, S.; Mathur, S. *Phys. Rev. B* **2007**, *76*, 85429.
(10) Hernandez-Ramirez, F.; Tarancon, A.; Casals, O.; Arbiol, J.; Romano-Rodriguez, A.; Morante, J. *Sens. Actuators, B* **2007**, *121*, 3–17.
(11) Malagu, C.; Guidi, V.; Stefancich, M.; Carotta, M. C.; Martinelli, G. *J. Appl. Phys.* **2002**, *91*, 808–814.
(12) Tian, B. Z.; Liu, X. Y.; Yang, H. F.; Xie, S. H.; Yu, C. Z.; Tu, B.; Zhao, D. Y. *Adv. Mater.* **2003**, *15*, 1370–1374.
(13) Laha, S. C.; Ryoo, R. *Chem. Commun.* **2003**, 2138–2139.

Published on Web 04/29/2010

walls by the so-called nanocasting route.[12−29] In this route, mesoporous silica with a three-dimensional pore network such as SBA-15[30,31] (derived from the surfactant templates) was usually used as the "hard template". The solution-based precursor of the desired metal oxide is introduced into the void mesoporous channel of silica. Subsequent heating to form the desired crystalline metal oxides and removal of the silica template could leave a negative mesoporous replica of the desired metal oxide, which is substantially an ordered array of metal oxide nanorods or nanowires and inversely replicated from the ordered structure of mesoporous silica. Their ultrathin nanorod diameter and accessible pores among nanorods make them particularly suitable as sensor materials. For example, various gas sensors based on tungsten oxide nanowire arrays have been fabricated.[32,33] Some examples of indium oxide nanowire arrays have also been reported.[34,35] Indium oxide is a well-known semiconducting sensing material for detection of low concentrations of oxidizing gases like O_3,[36−39] O_2,[40] NO_x,[7,41,42] and reducing gases like CO,[7] H_2,[43,44] and NH_3.[45] In previous work, In_2O_3 nanowire arrays with large specific surface areas have been synthesized with microwave-digested or calcined mesoporous silica as the template.[34,35,46] Tiemann's group[34] and Pellicer's group[47] also reported the improved response of In_2O_3 nanowire arrays to CH_4 and CO_2, respectively. However, the investigation of the influence of the pore interconnectivity and size of the silica template and loading of the indium source on the resultant In_2O_3 replica as well as their response to HCHO is still rare.

Herein, we report on the synthesis of ordered mesostructured In_2O_3 nanorod arrays using mesoporous silica (SBA-15) with different pore sizes as a template, where the expensive organic template in SBA-15 is nondestructively removed via solvent extraction and is acceptable for their recovery and reuse, which may be especially favorable for the reduction of costs in real applications. The influence of pore size and interconnectivity and of the silica template and loading of the indium source were investigated. The gas sensing test results show that the mesostructured In_2O_3 is very sensitive to HCHO, even at very low concentrations. The response intensity of mesostructured In_2O_3 to 10 ppm HCHO is up to 10.6, significantly higher than those of previously reported indium oxide-based sensors.[48]

Experimental Section

Synthesis. Mesoporous silica was prepared under hydrothermal conditions of 100 °C for 1 day, 130 °C for 1 day, and 130 °C for 5 days, according to the established procedures.[49] The template was removed by solvent extraction with a hydrochloric acid/ethanol solution. The resultant silica species were termed SBA-15-*x*-*y*, where *x* stands for the hydrothermal aging temperature and *y* stands for time. In_2O_3/SiO_2 composites and the pure In_2O_3 samples were termed In_2O_3@SBA-15-*x*-*y*-*z* and In_2O_3-*x*-*y*-*z*, where *z* stands for the loading of the indium source. Loading values are given as volume percents of the accessible pore volume filled with In_2O_3, assuming the bulk density of In_2O_3 for the indium oxide in the pore system; 0.6 g of SBA-15 was dispersed in 10 g of an ethanol solution containing 1.8 g of hydrated indium nitrate and then stirred at 40 °C until that ethanol was evaporated. Afterward, the resulting powder was heated in a ceramic crucible in an oven at 250 °C for 4 h, to decompose indium nitrate. The filling and heating steps were

(14) Tian, B. Z.; Liu, X. Y.; Solovyov, L. A.; Liu, Z.; Yang, H. F.; Zhang, Z. D.; Xie, S. H.; Zhang, F. Q.; Tu, B.; Yu, C. Z.; Terasaki, O.; Zhao, D. Y. *J. Am. Chem. Soc.* **2004**, *126*, 865–875.
(15) Wang, Y. Q.; Yang, C. M.; Schmidt, W.; Spliethoff, B.; Bill, E.; Schuth, F. *Adv. Mater.* **2005**, *17*, 53–56.
(16) Jiao, F.; Harrison, A.; Jumas, J. C.; Chadwick, A. V.; Kockelmann, W.; Bruce, P. G. *J. Am. Chem. Soc.* **2006**, *128*, 5468–5474.
(17) Rumplecker, A.; Kleitz, F.; Salabas, E. L.; Schuth, F. *Chem. Mater.* **2007**, *19*, 485–496.
(18) Yue, W. B.; Zhou, W. Z. *J. Mater. Chem.* **2007**, *17*, 4947–4952.
(19) Zhou, L.; Ren, Q. J.; Zhou, X. F.; Tang, J. W.; Chen, Z. H.; Yu, C. Z. *Microporous Mesoporous Mater.* **2008**, *109*, 248–257.
(20) Zheng, M. B.; Cao, J.; Liao, S. T.; Liu, J. S.; Chen, H. Q.; Zhao, Y.; Dai, W. J.; Ji, G. B.; Cao, J. M.; Tao, J. *J. Phys. Chem. C* **2009**, *113*, 3887–3894.
(21) Roggenbuck, J.; Tiemann, M. *J. Am. Chem. Soc.* **2005**, *127*, 1096–1097.
(22) Liu, Q.; Wang, A. Q.; Wang, X. D.; Zhang, T. *Chem. Mater.* **2006**, *18*, 5153–5155.
(23) Lai, X. Y.; Li, X. T.; Geng, W. C.; Tu, J. C.; Li, J. X.; Qiu, S. L. *Angew. Chem., Int. Ed.* **2007**, *46*, 738–741.
(24) Roggenbuck, J.; Schafer, H.; Tsoncheva, T.; Minchev, C.; Hanss, J.; Tiemann, M. *Microporous Mesoporous Mater.* **2007**, *101*, 335–341.
(25) Polarz, S.; Orlov, A. V.; Schuth, F.; Lu, A. H. *Chem.—Eur. J.* **2007**, *13*, 592–597.
(26) Kim, H.; Cho, J. *J. Mater. Chem.* **2008**, *18*, 771–775.
(27) Liu, B.; Baker, R. T. *J. Mater. Chem.* **2008**, *18*, 5200–5207.
(28) Tuysuz, H.; Liu, Y.; Weidenthaler, C.; Schuth, F. *J. Am. Chem. Soc.* **2008**, *130*, 14108–14110.
(29) Lai, X. Y.; Wang, H.; Mao, D.; Yang, N. L.; Yao, J. X.; Xing, C. J.; Wang, D.; Li, X. T. *Mater. Lett.* **2008**, *62*, 3868–3871.
(30) Zhao, D. Y.; Huo, Q. S.; Feng, J. L.; Chmelka, B. F.; Stucky, G. D. *J. Am. Chem. Soc.* **1998**, *120*, 6024–6036.
(31) Lee, J. S.; Joo, S. H.; Ryoo, R. *J. Am. Chem. Soc.* **2002**, *124*, 1156–1157.
(32) Rossinyol, E.; Prim, A.; Pellicer, E.; Arbiol, J.; Hernández-Ramírez, F.; Peiró, F.; Cornet, A.; Morante, J.; Solovyov, L.; Tian, B. *Adv. Funct. Mater.* **2007**, *17*, 1801.
(33) Rossinyol, E.; Arbiol, J.; Peiró, F.; Cornet, A.; Morante, J.; Tian, B.; Bo, T.; Zhao, D. *Sens. Actuators, B* **2005**, *109*, 57–63.
(34) Waitz, T.; Wagner, T.; Sauerwald, T.; Kohl, C. D.; Tiemann, M. *Adv. Funct. Mater.* **2009**, *19*, 653–661.
(35) Wagner, T.; Sauerwald, T.; Kohl, C. D.; Waitz, T.; Weidmann, C.; Tiemann, M. *Thin Solid Films* **2009**, *517*, 6170–6175.
(36) Gurlo, A.; Barsan, N.; Weimar, U.; Ivanovskaya, M.; Taurino, A.; Siciliano, P. *Chem. Mater.* **2003**, *15*, 4377–4383.
(37) Epifani, M.; Comini, E.; Arbiol, J.; Diaz, R.; Sergent, N.; Pagnier, T.; Siciliano, P.; Faglia, G.; Morante, J. R. *Sens. Actuators, B* **2008**, *130*, 483–487.
(38) Ivanovskaya, M.; Gurlo, A.; Bogdanov, P. *Sens. Actuators, B* **2001**, *77*, 264–267.
(39) Korotcenkov, G.; Cerneavschi, A.; Brinzari, V.; Vasiliev, A.; Ivanov, M.; Cornet, A.; Morante, J.; Cabot, A.; Arbiol, J. *Sens. Actuators, B* **2004**, *99*, 297–303.
(40) Neri, G.; Bonavita, A.; Micali, G.; Rizzo, G.; Pinna, N.; Niederberger, M. *Sens. Actuators, B* **2007**, *127*, 455–462.
(41) Wang, C. Y.; Ali, M.; Kups, T.; Rohlig, C. C.; Cimalla, V.; Stauden, T.; Ambacher, O. *Sens. Actuators, B* **2008**, *130*, 589–593.
(42) Xu, P. C.; Cheng, Z. X.; Pan, Q. Y.; Xu, J. Q.; Xiang, Q.; Yu, W. J.; Chu, Y. L. *Sens. Actuators, B* **2008**, *130*, 802–808.
(43) Chung, W. Y.; Sakai, G.; Shimanoe, K.; Miura, N.; Lee, D. D.; Yamazoe, N. *Sens. Actuators, B* **1998**, *46*, 139–145.
(44) Zhan, Z.; Jiang, D.; Xu, J. *Mater. Chem. Phys.* **2005**, *90*, 250–254.
(45) Du, N.; Zhang, H.; Chen, B. D.; Ma, X. Y.; Liu, Z. H.; Wu, J. B.; Yang, D. R. *Adv. Mater.* **2007**, *19*, 1641–1645.
(46) Yang, H. F.; Shi, Q. H.; Tian, B. Z.; Lu, Q. Y.; Gao, F.; Xie, S. H.; Fan, J.; Yu, C. Z.; Tu, B.; Zhao, D. Y. *J. Am. Chem. Soc.* **2003**, *125*, 4724–4725.
(47) Prim, A.; Pellicer, E.; Rossinyol, E.; Peiro, F.; Cornet, A.; Morante, J. R. *Adv. Funct. Mater.* **2007**, *17*, 2957–2963.
(48) Li, E.; Cheng, Z.; Xu, J.; Pan, Q.; Yu, W.; Chu, Y. *Cryst. Growth Des.* **2009**, *9*, 2146–2151.
(49) Sayari, A.; Han, B. H.; Yang, Y. *J. Am. Chem. Soc.* **2004**, *126*, 14348–14349.

Table 1. Textural Properties of Mesostructured Products

product	lattice parameter[a] (nm)	BET specific surface area (m^2/g)	pore size (nm)	pore volume (cm^3/g)	residual Si content[b] (wt %)
SBA-15-100-1d	12.4	714	7.0	0.93	–
SBA-15-130-1d	12.3	478	8.8	1.00	–
SBA-15-130-5d	12.3	363	11.3	1.21	–
In_2O_3@SBA-15-130-1d-15	11.6	256	8.4	0.44	–
In_2O_3@SBA-15-130-1d-27	11.6	206	8.1	0.31	–
In_2O_3@SBA-15-130-1d-35	11.6	144	8.0	0.22	–
In_2O_3-130-1d-15	–	91	2.5	0.41	0.1
In_2O_3-130-1d-27	11.6	126	3.8	0.42	1.2
In_2O_3-130-1d-35	11.6	53	3.7	0.21	0.9
In_2O_3-130-5d-22	11.8	70	6.5	0.25	0.3
In_2O_3-130-5d-29	11.7	70	4.8	0.26	0.4

[a] Calculated from the d_{100} spacing in the XRD patterns. [b] Determined by ICP-OES after acid digestion (hydrochloric and hydrofluoric acid).

repeated twice following the same conditions to achieve higher loadings, except for the amounts of indium nitrate were decreased to 1.4 and 1.0 g. Finally, the silica template was then removed at room temperature using a 2 M NaOH aqueous solution. The yellow indium oxide material was recovered by centrifugation and dried at 70 °C overnight. ICP-OES measurement reveals almost complete removal of the silica template (Table 1). Moreover, bulk indium oxide particles were also prepared by direct decomposition of indium nitrate without templates at 500 °C.

Characterization. The powder X-ray diffraction (XRD) patterns were recorded with an X'Pert PRO MPD [Cu Kα (λ = 1.5405 Å) radiation], operating at 30 mA and 40 kV. The nitrogen adsorption−desorption isotherms at the temperature of liquid nitrogen (77 K) were measured on a Quantochrome Autosorb-1 sorption analyzer with prior degassing under vacuum at 200 °C overnight. Total pore volumes were determined using the adsorbed volume at a relative pressure of 0.99. The multipoint Brunauer−Emmet−Teller (BET) surface area was estimated from the relative pressure range from 0.05 to 0.2. The pore size distribution of all mesostructured materials was analyzed using the Barrett−Joyner−Halenda (BJH) algorithm except for mesoporous silica materials, for which nonlocal density functional theory (NLDFT) methods were used. FTIR spectra were recorded on a FTIR spectrometer (Bruker Equniox 55) using the KBr wafer technique. Scanning electron microscopy (SEM) images were obtained with a JSM-6700 instrument, operating at 5.0 kV. Transmission electron microscopy (TEM) images and high-resolution transmission electron microscopy (HRTEM) images were recorded with a JEOL JEM-2100F instrument, operating at an acceleration voltage of 200 kV. Chemical analysis was conducted by ICP-OES (Optima 5300DV, PerkinElmer).

Sensing Test. We fabricated the gas sensors by coating indium oxide samples on a quartz substrate as a sensing layer. Indium oxide samples were dispersed in ethanol under ultrasonic stimuli, and the resultant suspension was dropped on the quartz substrate. After the evaporation of ethanol, the indium oxide sensing layer formed on the quartz substrate was annealed at 300 °C for 1 h. The gas sensing test was performed in an apparatus (Figure S1 of the Supporting Information). Ag paste and Pt wires were used to connect the gas sensing layer with an amperemeter (Keithley 2601, Keithley Instrument Inc.), and the DC voltage was fixed at 5 V. The electrical response of the sensor was measured with an automatic test system, controlled by a personal computer.

Results and Discussion

The N_2 sorption analysis results of all the extracted SBA-15 samples are shown in Figure 1. Clearly, the hysteresis

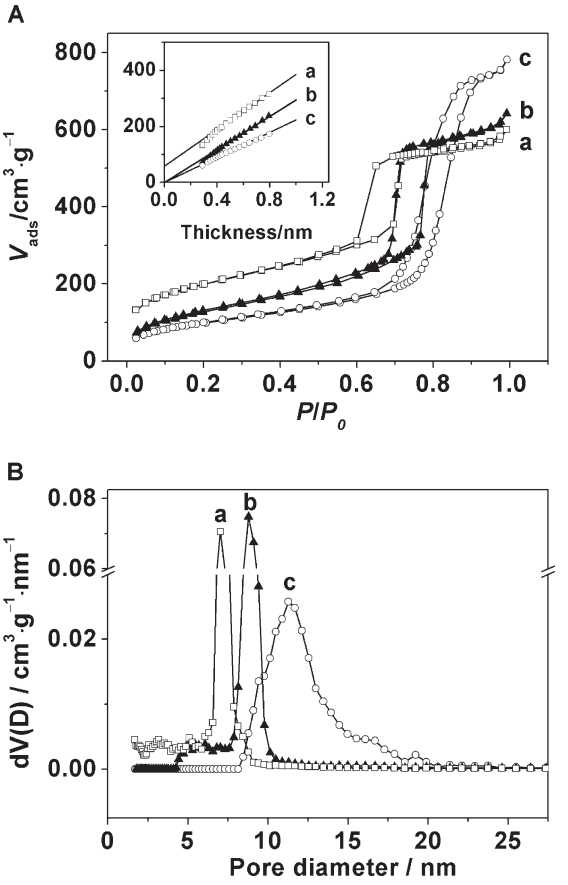

Figure 1. (A) Nitrogen physisorption isotherms of (a) SBA-15-100-1d, (b) SBA-15-130-1d, and (c) SBA-15-130-5d (the insets are the corresponding *t*-plots) and (B) corresponding pore size distributions.

loop observed for two silica species synthesized under hydrothermal conditions of 130 °C occurs at much higher relative pressures compared to that of the equivalent obtained at 100 °C (Figure 1A), indicating much larger mesopore dimensions, a fact also substantiated by the pore size distributions calculated by the density functional theory (DFT) method (Figure 1B). The *t*-plots of SBA-15-130-1d and SBA-15-130-5d pass zero of axis, meaning no micropore in the two silica species, whereas SBA-15-100-1d has a substantial fraction of micropores (microporous volume of ~0.09 cm^3/g). Also, the pore size distributions calculated by DFT suggest that SBA-15-130-1d did not contain pores smaller than 4 nm and SBA-15-130-5d did not contain

pores smaller than 8 nm. Therefore, we speculate that a relatively high-temperature hydrothermal treatment could indeed enlarge not only the primary mesopore of mesoporous silica but also the secondary pore within the silica walls and improve its pore interconnectivity.[50] IR spectra (Figure S2 of the Supporting Information) reveal that SBA-15-100-1d still contains a certain amount of surfactants after the extraction treatment, consistent with the previous reports,[51] and the surfactants in two silica species obtained at 130 °C have been completely removed after the same treatment. Therefore, there is no need for the latter to do an extra calcination or oxidation treatment, which usually has to be done for the former to remove the remaining surfactants. The difference may derive from the fact that two silica species obtained at 130 °C possess larger pores than that obtained at 100 °C, and therefore, more solvent molecules could come into the pores to interact with the surfactant molecules and finally "drag" them out from the pores. Moreover, we also noted that the pore size distribution of SBA-15-130-5d is much wider than those of two other silica species, suggesting overly long hydrothermal treatment may damage the mesostructure of mesoporous silica. That is also confirmed by the low-angle XRD pattern of SBA-15-130-5d (Figure S3 of the Supporting Information), which exhibits characteristic diffraction peaks with an intensity relatively lower than those of other silica species.

SBA-15-130-1d was first chosen as a template for the In_2O_3 replica. Indium oxide was loaded in the mesoporous silica by the filling and heating steps. In general, the rate of loading of metal oxides in the mesopore channels of the templates is a key point for the production of high-quality replica materials. Rumplecker et al. reported that the threshold loading for the successful nanocasting of Co_3O_4 from calcined SBA-15 is ~17%.[17] However, there are no directly available loading data for In_2O_3. In this paper, the influence of loading (15, 27, and 35%) of indium oxide to SBA-15 was examined, and higher loadings were achieved by repeating the filling and heating steps. The loading of In_2O_3 in the silica was monitored with nitrogen physisorption measurements performed after each step of filling and heating (Figure 2). The specific pore volume (i.e., the integrated peak area) decreases from 1.00 cm^3/g to 0.42, 0.31, and 0.22 cm^3/g after the filling and heating steps are repeatedly performed (Table 1), implying the loading of In_2O_3 in the mesopores. From the low-angle XRD patterns of In_2O_3/SiO_2 composites (Figure 3), one can see that the intensity of characteristic diffraction peaks markedly decreased with repetition of the filling and heating steps. This can usually be interpreted as a reduction in the X-ray scattering contrast between the pore and framework of the mesoporous silica, caused by the presence of heavy metal atoms inside the silica mesochannels. These results suggest that indium oxides were indeed loaded into the mesochannels of SBA-15-130-1d.

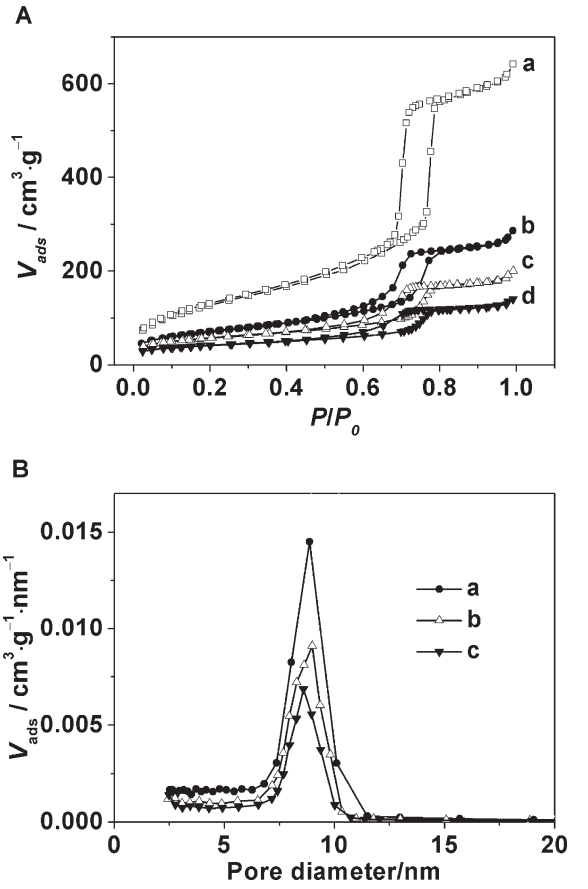

Figure 2. (A) Nitrogen physisorption isotherms of (a) In_2O_3@SBA-15-130-1d-15, (b) In_2O_3@SBA-15-130-1d-27, and (c) In_2O_3@SBA-15-130-1d-35 and (B) corresponding pore size distributions.

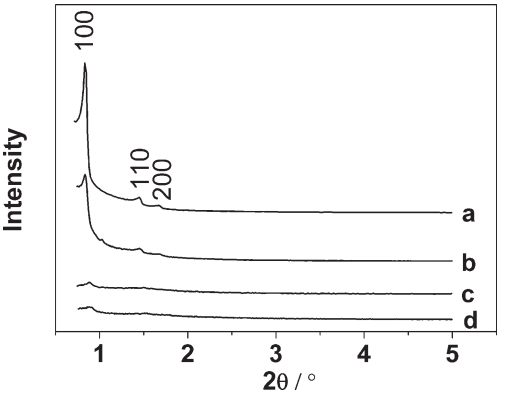

Figure 3. Low-angle XRD pattern of (a) SBA-15-130-1d, (b) In_2O_3@SBA-15-130-1d-15, (c) In_2O_3@SBA-15-130-1d-27, and (d) In_2O_3@SBA-15-130-1d-35.

All pure In_2O_3 samples obtained after dissolution of the silica were analyzed with XRD, TEM, SEM, and nitrogen physisorption. The XRD analysis results show that only In_2O_3-130-1d-35 among three In_2O_3 replicas templated from In_2O_3-130-1d exhibits three characteristic diffraction peaks of two-dimensional (2D) hexagonal *p6mm* structure (Figure 4b). The symmetry corresponds to the silica template (SBA-15-130-1d), with even the higher-order diffraction peaks [(110) and (200)] being well-resolved, thus indicating excellent replication of SBA-15 into highly

(50) Choi, M.; Heo, W.; Kleitz, F.; Ryoo, R. *Chem. Commun.* **2003**, 1340–1341.
(51) Tian, B. Z.; Liu, X. Y.; Yu, C. Z.; Gao, F.; Luo, Q.; Xie, S. H.; Tu, B.; Zhao, D. Y. *Chem. Commun.* **2002**, 1186–1187.

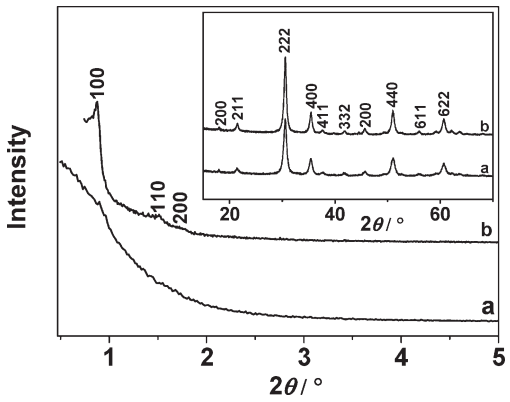

Figure 4. Low-angle and wide-angle (inset) XRD patterns of (a) In_2O_3-SBA-1d-27 and (b) In_2O_3-130-1d-35.

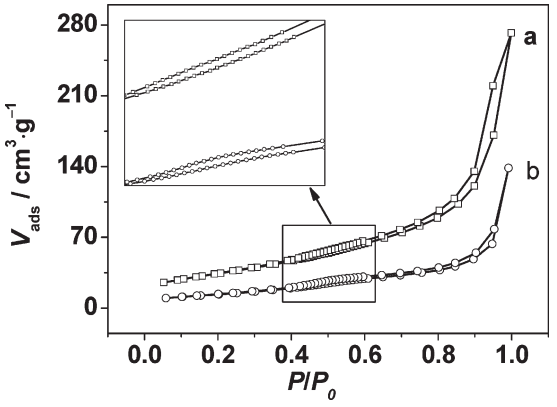

Figure 5. Nitrogen physisorption isotherms of (a) In_2O_3-130-1d-27 and (b) In_2O_3-130-1d-35.

ordered 2D hexagonal indium oxide. On the other hand, only very weak diffraction peaks could be observed in the low-angle XRD pattern of In_2O_3-130-1d-27 (Figure 4a), and In_2O_3-130-1d-15 does not exhibit any diffraction peaks in its low-angle XRD pattern (not shown), suggesting they may possess less ordered or disordered mesostructure. All In_2O_3 replicas (insets of Figure 4) show the characteristic wide-angle X-ray diffraction peaks in accordance with the cubic In_2O_3 phase (JCPDS Card 65-3170), suggesting crystalline products were obtained.

In_2O_3-130-1d-35 gave a typical type IV isotherm with a clear H1-type hysteresis loop (Figure 5b), which is characteristic for mesoporous materials. It is noticeable that the type of hysteresis clearly resembles the hysteresis observed for an ordered mesoporous carbon replica (CMK-3),[52] suggesting they possess similar mesostructures. Two well-defined steps of capillary condensation (P/P_0 = 0.4−0.6 and 0.8−1.0) could also be observed. The former is caused by the adsorption of the mesopores, and a narrow pore size distribution (average pore size of 3.7 nm) confirms the highly ordered uniform pore structure (Figure 6b). The latter consists of an appreciable fraction of textural porosity. The specific surface area and the total pore volume of the In_2O_3 replica were calculated from the

(52) Jun, S.; Joo, S. H.; Ryoo, R.; Kruk, M.; Jaroniec, M.; Liu, Z.; Ohsuna, T.; Terasaki, O. *J. Am. Chem. Soc.* **2000**, *122*, 10712–10713.

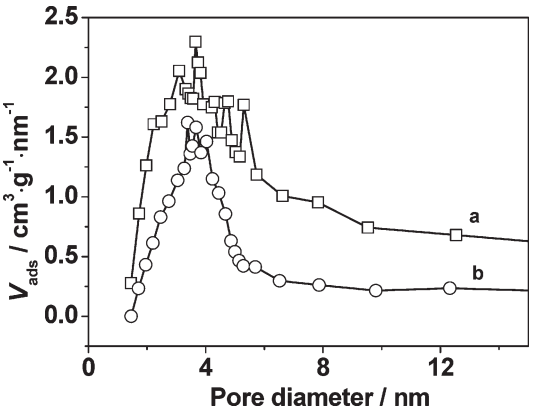

Figure 6. Pore size distributions of (a) In_2O_3-130-1d-27 and (b) In_2O_3-130-1d-35.

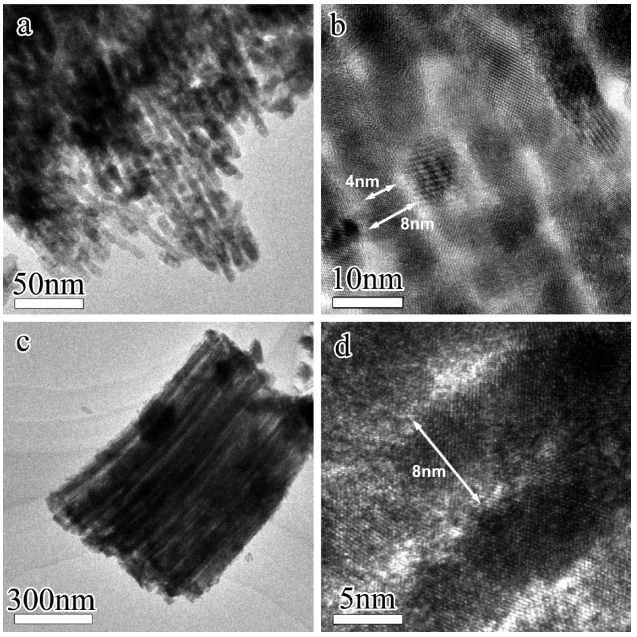

Figure 7. TEM images of (a and b) In_2O_3-130-1d-27 and (c and d) In_2O_3-130-1d-35.

physisorption results to be 53 m^2/g and 0.21 cm^3/g. In_2O_3-130-1d-27 exhibited a quite different isotherm with a wide pore size distribution (Figures 5a and 6a), possibly related to its less ordered mesostructure. Nevertheless, In_2O_3-130-1d-27 possesses a much larger specific surface area (126 m^2/g) and a larger total pore volume (0.42 cm^3/g) than In_2O_3-130-1d-35.

The TEM image (Figure 7c) reveals that In_2O_3-130-1d-35 has a rodlike morphology with particle sizes of 0.6−0.9 μm, and the whole particle is an ordered array of nanorods separated by a constant repeat distance. These arrays reflect the pore topology of the template material SBA-15. In the In_2O_3-130-1d-35 sample, nanorods of In_2O_3 with a diameter of 8.0 nm were observed. The parent silica SBA-15 consists of mesopores with a diameter of 8.8 nm, determined using the NLDFT method; this value is in reasonable agreement with the nanorod diameter, considering the uncertainties both in the determination of the pore size and in the exact determination of the nanorod diameters in the TEM as well as the possible pore reduction

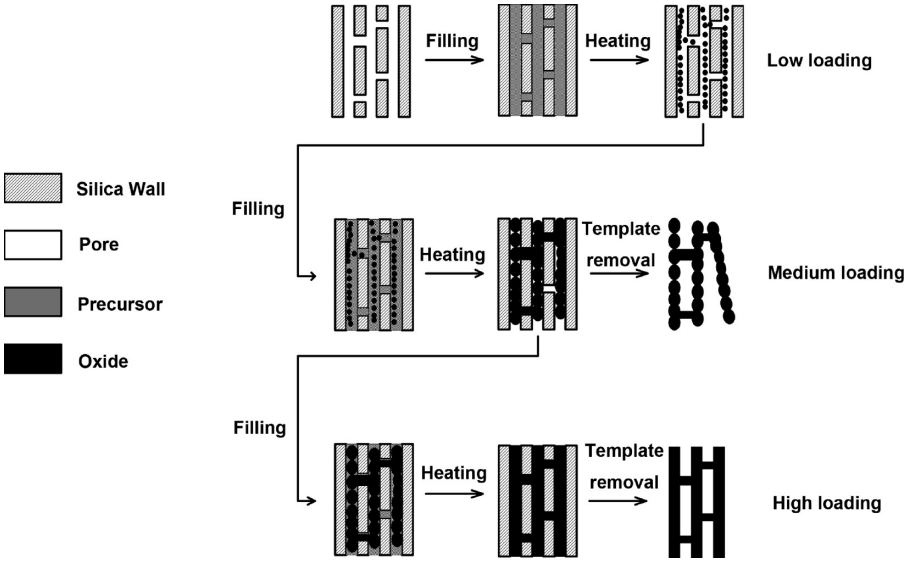

Figure 8. Schematic representation of the formation of mesostructured indium oxide in the channels of SBA-15.

caused by lattice shrinkage during thermal treatment (Table 1). Different from In_2O_3-130-1d-35, In_2O_3-130-1d-27 consists of less-ordered nanorod arrays, and most of the nanorods are in a disordered arrangement (Figure 7a). Interestingly, nanorods in In_2O_3-130-1d-27 exhibit a special morphology and look like chains of connected nanobeads, with the different diameter (4−8 nm) at different positions of one nanorod. Maybe that is the reason that In_2O_3-130-1d-27 exhibits a much larger specific surface area and a larger total pore volume.

Normally, the nucleation and growth of indium oxide from an indium nitrate precursor would lead to the formation of bulk particles at high temperatures, but in the case of the nanocasting procedure, the pore walls could not only limit the diffusion of the precursor but also prevent the further growth of the indium oxide crystals. Therefore, in the case of single filling, especially with a smaller loading of the precursor, the nucleation and growth usually took place at many different positions of channel of mesoporous silica and then easily formed some separated nanoparticles (normally possessing a beadlike morphology, because of its minimum free energy).[53] By repeating the filling and heating to achieve a high loading, these nanoparticles would further grow and connect together, forming bead-chain-like nanorods. When the size of indium oxide crystals is close to the mesopore dimension of the silica template, the growth of the crystal in the direction vertical to mesochannels would be prevented by pore walls and only the growth along the mesochannels is allowed, which would result in the indium oxide crystal completely occupying the cylindrical mesochannels in the partial or even whole domain of silica particles forming uniform nanorods. From the high-resolution TEM images (Figure 7b,d), it is clear that each nanorod is composed of numerous single crystals with the different lattice growth orientations, to some degree confirming the speculation mentioned above. Moreover, the nanorods formed by decomposition of the precursors would also extend from the primary mesopore to the connecting pore within the walls during the further growth process, and then the adjacent nanorods would be connected through the "nanoconnector" formed in connecting pores. If there are enough nanoconnectors among the nanorods, the ordered arrangement of nanorods could be kept after template removal. Otherwise, only less ordered arrays of nanorods or individual nanorods would be obtained. Therefore, a higher loading would be required to form enough nanoconnectors among the nanorods and produce the ordered nanorod arrays. According to the results discussed above, a loading of ~27%, an even higher value seems to be necessary for SBA-15-130-1d to produce indium oxide nanorod array materials reflecting the 2D hexagonal symmetry of the template. These nanorod arrays are also expected to provide a better mechanical stability than individual nanorods or nanoparticles, and the confined growth of indium oxide in the pores of SBA-15 is illustrated in Figure 8.

Moreover, improving the pore interconnectivity of mesoporous silica may weaken the limiting effect of pore walls on the diffusion of the precursor and facilitate the formation of a nanoconnector. To investigate the influence of pore interconnectivity, we also synthesized indium oxide replicas by using SBA-15-130-5d under the same conditions, including the amount of precursor, the filling and heating process, etc. Because of the larger specific pore volume of SBA-15-130-5d, the corresponding loading achieved by the same nanocasting process will be lower than that for SBA-15-130-1d. The low-angle XRD pattern of In_2O_3-130-5d-22 (Figure 9a) exhibits an intense diffraction peak and two weak peaks, suggesting that it possesses the highly ordered mesostructure. In other words, we could obtain an ordered replica by using SBA-15-130-5d at a relatively lower loading. Moreover, we also observed that In_2O_3-130-5d-29 (Figure 9b) also exhibits three diffraction peaks, but its higher-order diffraction peaks

(53) Kockrick, E.; Krawiec, P.; Schnelle, W.; Geiger, D.; Schappacher, F. M.; Pottgen, R.; Kaskel, S. *Adv. Mater.* **2007**, *19*, 3021–3026.

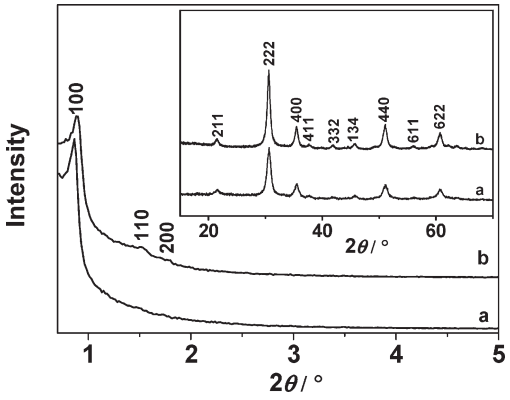

Figure 9. Low-angle and wide-angle (inset) XRD patterns of (a) In_2O_3-130-5d-22 and (b) In_2O_3-130-5d-29.

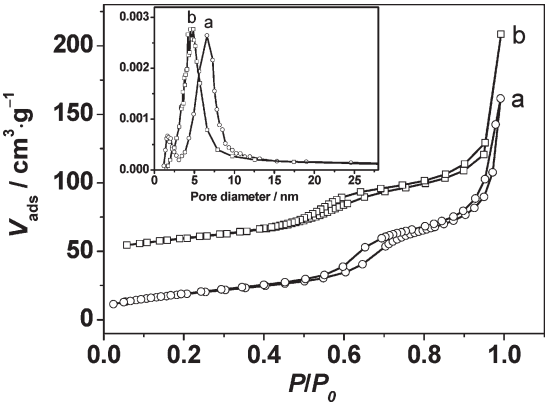

Figure 10. Nitrogen physisorption isotherms and corresponding pore size distributions (inset) of (a) In_2O_3-130-5d-22 and (b) In_2O_3-130-5d-29. For the sake of clarity, the data are given with an offset of 40 cm^3/g (In_2O_3-130-5d-29).

[(110) and (200)] are more resolved than those of In_2O_3-130-5d-22, suggesting the former possesses a more ordered mesostructure than the latter. Wide-angle XRD patterns (the insets of Figure 9) confirmed that the two species correspond to the cubic In_2O_3 phase (JCPDS Card 65-3170). Typical type IV isotherms (Figure 10) are detected for In_2O_3-130-5d-22 and In_2O_3-130-5d-29. In_2O_3-130-5d-22 has a pore volume of 0.25 cm^3/g and a specific surface area of 70 m^2/g, whereas In_2O_3-130-5d-29 possesses a pore volume of 0.26 cm^3/g and a specific surface area of 70 m^2/g.The SEM images (Figure 11a,b) reveal that In_2O_3-130-5d-22 and In_2O_3-130-5d-29 are composed of nanoparticles with a typical diameter of 50−200 nm, which is smaller than those of In_2O_3-130-1d-27 and In_2O_3-130-1d-35. The TEM image (Figure 11c,d) indicates that those nanoparticles are ordered arrays of nanorods, consistent with the low-angle XRD results. These nanorods are uniform in diameter (~9 nm), because of the confined growth in the channels of the silica template. These results reveal that we could realize the controllable synthesis of In_2O_3 replicas with different textural and morphological properties, by adjusting the template properties and the loading of indium precursors.

Formaldehyde (HCHO) is well-known as a colorless, strong-smelling, and toxic gas and is extremely dangerous

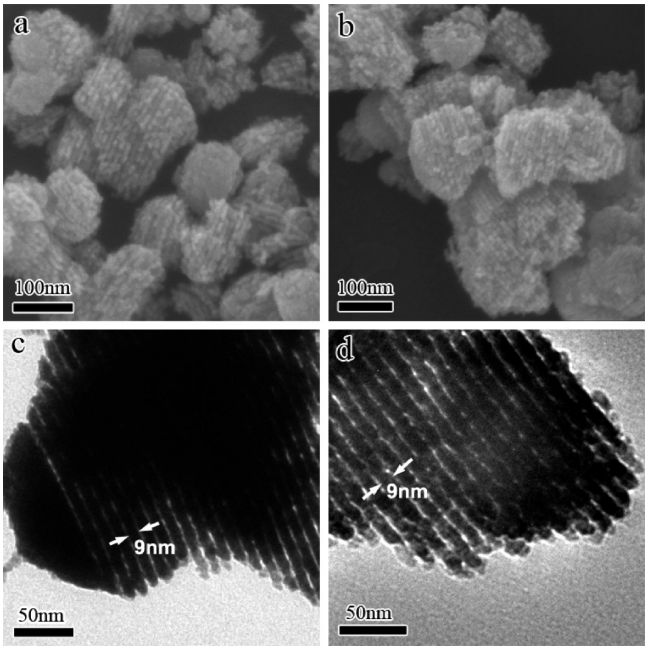

Figure 11. SEM and TEM images of (a and c) In_2O_3-130-5d-22 and (b and d) In_2O_3-15-130-5d-29.

to the human body.[54] Therefore, effective methods for monitoring formaldehyde are of great importance and are in great demand for both environmental protection and human health. Gas sensors based on semiconductor metal oxides such as SnO_2, In_2O_3, ZnO, and WO_3 provide the safe detection of toxic or flammable gases,[29,55−57] but they still have some limitations and challenges such as response, selectivity, long-term stability, etc. In general, the response of semiconductor gas sensors is related to the number of active sites on their surface, and increasing their specific surface area could generate more active sites and may improve their response.[58] Moreover, the fabrication and operation of sensors often occur under high-temperature conditions, and thus, the thermal stability of the sensing material has a great effect on the stability of sensor devices. Thermal stability testing results show that mesostructured In_2O_3 replicas could maintain their structures below 450 °C (Figure S4 of the Supporting Information). For those reasons, we fabricated a gas sensor for the detection of HCHO using the as-synthesized mesostructured indium oxides with large specific surface areas, and the bulk indium oxide particles were also used as a benchmark.

It is well-known that the response of a semiconductor gas sensor is strongly influenced by its operating temperature.[59,60] To determine optimum operating temperatures,

(54) Flueckiger, J.; Ko, F. K.; Cheung, K. C. *Sensors* **2009**, *9*, 9196–9215.
(55) Zeng, Y.; Zhang, T.; Wang, L. J.; Wang, R. *J. Phys. Chem. C* **2009**, *113*, 3442–3448.
(56) Liu, Y.; Koep, E.; Liu, M. L. *Chem. Mater.* **2005**, *17*, 3997–4000.
(57) Epifani, M.; Andreu, T.; Arbiol, J.; Diaz, R.; Siciliano, P.; Morante, J. R. *Chem. Mater.* **2009**, *21*, 5215–5221.
(58) Tiemann, M. *Chem.—Eur. J.* **2007**, *13*, 8376–8388.
(59) Liu, J. F.; Wang, X.; Peng, Q.; Li, Y. D. *Adv. Mater.* **2005**, *17*, 764–767.
(60) Zhang, G. Y.; Li, C. S.; Cheng, F. Y.; Chen, J. *Sens. Actuators, B* **2007**, *120*, 403–410.

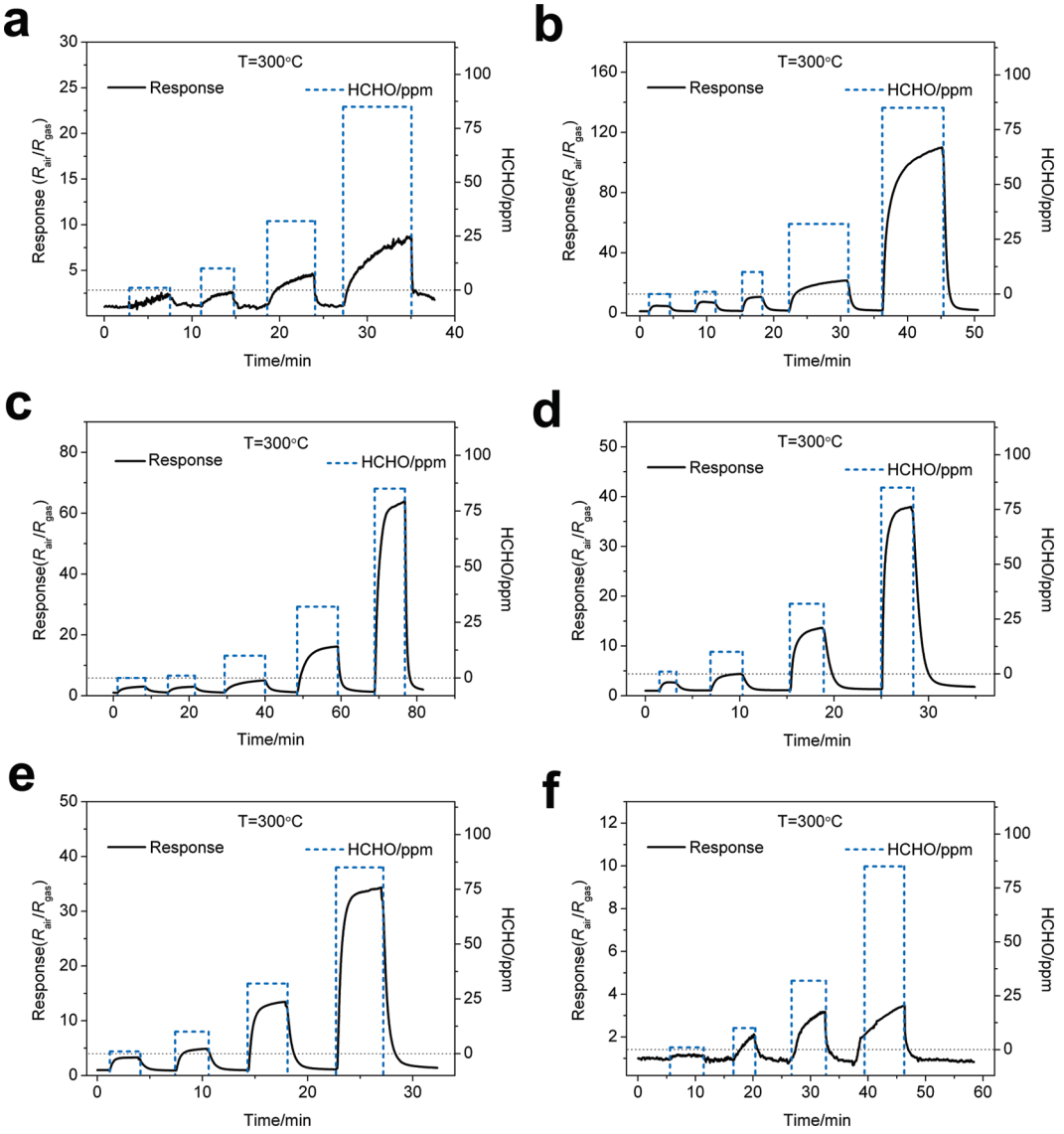

Figure 12. Typical dynamic response curves of gas sensors fabricated from (a) In_2O_3-15-130-1d-15, (b) In_2O_3-130-1d-27, (c) In_2O_3-130-1d-35, (d) In_2O_3-130-5d-22, (e) In_2O_3-130-5d-29, and (f) a bulk In_2O_3 particle, during cycling between increasing concentrations of HCHO and ambient air at 300 °C.

the response of gas sensors fabricated by two In_2O_3 samples (In_2O_3-130-1d-27 and In_2O_3-130-1d-35) to 32 ppm HCHO in air was tested as a function of operating temperature. Here, the sensor response (sensitivity) was defined as the ratio of resistance in air (R_{air}) to that in air containing HCHO gas (R_{gas}). As shown in Figure S5 of the Supporting Information, the strength of the response to HCHO increases with operating temperature to a maximum value located at ~300 °C and then decreases if the operating temperature is further increased. Therefore, the optimum operating temperature is 300 °C, and all further tests would be performed at this temperature.

The curves for the dynamic response to HCHO for all the sensors are depicted in Figure 12. Response and recovery times of all the sensors (defined as the time needed to reach 90% of the final equilibrium value) are calculated from the case of 32 ppm HCHO (Figure S6 of the Supporting Information), which depend largely upon the diffusion of HCHO within the sensing layer. Knudsen diffusion is the main diffusion type for the smaller pore (several nanometers), which gives a diffusion coefficient depending linearly on pore size.[58] Therefore, the smaller pores are unfavorable for the diffusion of HCHO. In_2O_3-130-1d-15 nanoparticles (including minute nanorods) lack substantial "support", easily suffered from grain growth during high-temperature thermal treatment,[34] and formed a relatively denser sensing layer with smaller pores of ~2.5 nm (Figure S7 of the Supporting Information), which makes the diffusion of HCHO within the sensing layer comparably hard and thus results in longer response and recovery times (276 and 65 s, respectively), compared with those of indium oxide bulk particles (242 and 63 s, respectively) with larger interparticle textural pores. For nanorod arrays, the diffusion of HCHO within them is thought to be relatively easier, since they possess larger particles and result in larger interparticle textural pores. However, the diffusion of HCHO within the intraparticle pores among the nanorods also needs to be considered, and larger intraparticle pores and shorter pore channels facilitate the transfer of HCHO. Therefore,

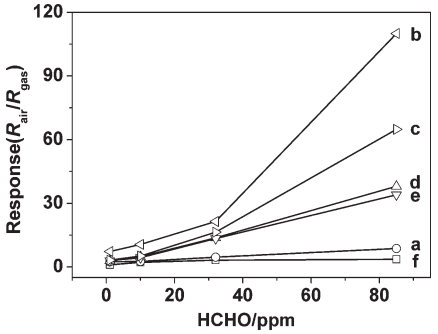

Figure 13. Response vs HCHO concentration of gas sensors fabricated from (a) In_2O_3-130-1d-15, (b) In_2O_3-130-1d-27, (c) In_2O_3-130-1d-35, (d) In_2O_3-130-5d-22, (e) In_2O_3-130-5d-29, and (f) a bulk In_2O_3 particle.

In_2O_3-130-5d-22 (81 and 106 s, respectively) and In_2O_3-130-5d-29 (69 and 78 s, respectively) with larger pores and shorter pore channels exhibit relatively shorter response times, while In_2O_3-130-1d-27 (231 and 72 s, respectively) and In_2O_3-130-1d-35 (234 and 111 s, respectively) with smaller pores and longer pore channels exhibit relatively longer response times.

Figure 13 shows the correlation between the response of all the sensors and the concentration of HCHO. We could observe that all the sensors fabricated from mesostructured In_2O_3, especially In_2O_3-130-1d-27 (126 m^2/g), exhibited a response to HCHO over the entire testing concentration range (1−85 ppm) stronger than that of the In_2O_3 bulk particle (4 m^2/g), which is attributed to the former's large surface area that allows it to absorb more gas molecules and thus be more sensitive. Even if compared with those HCHO sensors reported previously,[61−64] the In_2O_3-130-1d-27-based sensor still possesses the considerable advantage in response (Table S1 of the Supporting Information). However, we also note that the response of those mesostructured In_2O_3 nanoparticles is not exactly proportional to their surface areas (Figure 14a). In_2O_3-130-1d-15 with a larger specific surface area (91 m^2/g) exhibited a weaker response of 8.7 to 85 ppm HCHO, and In_2O_3-130-1d-35 possesses a smaller specific surface area (53 m^2/g) but exhibits a stronger response of 65 to 85 ppm HCHO compared to those of In_2O_3-130-5d-22 (70 m^2/g) and In_2O_3-130-1d-29 (70 m^2/g). Strong correlations between the size of grains in the nanometer range and the response are well-known in the literature for granular materials such as SnO_2 prepared by sol−gel methods, and the ideal particle size should be close to twice its Debye length.[65,66] Singh et al. also reported that the sensor response of indium oxide nanoparticles becomes sharply stronger when the particle size is reduced

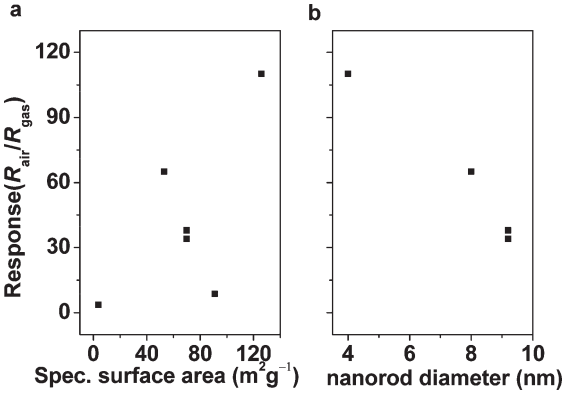

Figure 14. Correlation between the sensor signals shown in Figure 13 and structural parameters of the In_2O_3 samples. Response vs (a) the specific BET surface area and (b) the nanorod diameter.

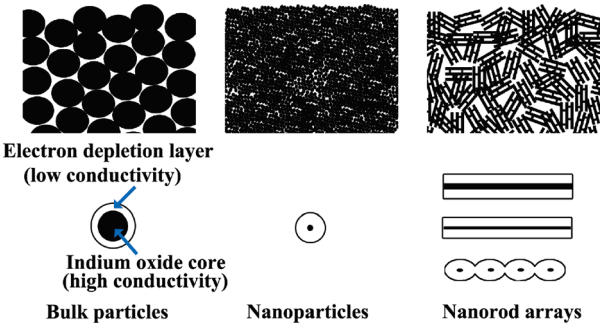

Figure 15. Illustration of the dependence of the response on the textural parameters of the sensing material.

from 29 to 5 nm.[67] Indium oxide possess a Debye length L (which corresponds to the electron-depleted layer width) of ~3 nm.[11,67] When the diameter of indium oxide is close to and even smaller than $2L$, a large fraction of the sensing layer will be involved in the charge transfer process, which will result in a strong response. Therefore, the poor response of bulk indium oxide particles is expectable, while In_2O_3-130-1d-15 may suffer from grain growth resulting from the high-temperature thermal treatment during the fabrication and operation of the sensor device and thus also exhibit a poor response. By analogy with nanoparticles, we can imagine that the conduction channel along indium oxide nanorods is very thin and small variations in the electron-depleted layer width caused by HCHO lead to strong effects on their electrical responses. For example, the diameter of nanorods in In_2O_3-130-1d-35 and In_2O_3-130-5d-22 is ca. 8 and 9 nm and the diameter of the corresponding conductivity channel only 2 and 3 nm, respectively. We could also induce that the nanorods with a thinner conductivity channel would exhibit larger conductivity variation for an equal variation in the electron-depleted layer width, which is in good agreement with our gas sensing test results. Especially, the nanorod in In_2O_3-130-1d-27 exhibits a bead-chain-like morphology, and the size of the nanorod at the thinnest position is ca. 4 nm, which means that the conduction channel is completely

(61) Xu, J. Q.; Ha, X. H.; Lou, X. D.; Xi, G. X.; Han, H. J.; Gao, Q. H. *Sens. Actuators, B* **2007**, *120*, 694–699.
(62) Gou, X. L.; Wang, G. X.; Yang, J. S.; Park, J.; Wexler, D. *J. Mater. Chem.* **2008**, *18*, 965–969.
(63) Lv, P.; Tang, Z. A.; Yu, J.; Zhang, F. T.; Wei, G. F.; Huang, Z. X.; Hu, Y. *Sens. Actuators, B* **2008**, *132*, 74–80.
(64) Wang, J. X.; Zou, B.; Ruan, S. P.; Zhao, J.; Wu, F. Q. *Mater. Chem. Phys.* **2009**, *117*, 489–493.
(65) Xu, C. N.; Tamaki, J.; Miura, N.; Yamazoe, N. *Sens. Actuators, B* **1991**, *3*, 147–155.
(66) Ansari, S. G.; Boroojerdian, P.; Sainkar, S. R.; Karekar, R. N.; Aiyer, R. C.; Kulkarni, S. K. *Thin Solid Films* **1997**, *295*, 271–276.
(67) Singh, V. N.; Mehta, B. R.; Joshi, R. K.; Kruis, F. E. *J. Nanosci. Nanotechnol.* **2007**, *7*, 1930–1934.

depleted in the partial region of the nanorod (Figure 15). The variation in the electron-depleted layer width caused by HCHO probably resulted in a "switch" effect in the electron transmission along the nanorods, and In_2O_3-130-1d-27 nanorod arrays thus exhibit a very strong response to HCHO (Figure 14b).

Conclusion

In summary, ordered mesostructured In_2O_3 nanorod arrays could be synthesized directly using extracted silica (SBA-15) as a template without any extra calcination or oxidation treatment via the nanocasting route. Depending on the template properties and the appropriate loading, mesostructured In_2O_3 replicas with controllable textural and morphological properties are accessible. The responses toward HCHO of the resultant ordered bead-chain-like In_2O_3 nanorod arrays were found to be very strong even at relatively lower levels, and such materials might be useful in detecting HCHO. Besides the specific surface area, the gas sensing properties prove to be influenced by other textural parameters of mesostructured sensors such as nanorod diameter, pore size, pore channel length, etc. Investigating the dependence of the gas response on the textural parameters of the mesostructured In_2O_3 nanorod array provides new inspiration for designing and fabricating gas sensors with tunable properties. A similar strategy could also be applied to other metal oxides such as tin oxide and indium−tin composite oxide (ITO), which themselves are also well-known semiconductor gas sensor materials. Further exploration of the possibly improving gas sensing properties of those metal oxides in the form of ordered mesostructured nanorod arrays will be worthwhile.

Acknowledgment. We thank Prof. Lin Guo for valuable help in recording the TEM images and Dr. Ning Wang for helpful discussion (Beijing University of Aeronautics and Astronautics). This work was partly supported by the National Natural Science Foundation of China (Grants 20401015, 20971125, and 50574082) and the Beijing Municipal Natural Science Foundation (Grant 2082022). D.W. thanks the "Century Program or Hundreds-Talent Program" of the Chinese Academy of Sciences.

Supporting Information Available: Gas sensor testing details, FTIR spectrum and XRD patterns of mesoporous silica, thermal stability test of In_2O_3-130-5d-29, temperature-dependent response curves of In_2O_3 sensors, response transients of the In_2O_3 sensors, nitrogen physisorption of In_2O_3-130-1d-15, and comparison of responses of various HCHO sensors. This material is available free of charge via the Internet at http://pubs.acs.org.